SUPPORTING INFORMATION

Fast Assembly of Gold Nanoparticles in Large-Area 2-D Nanogrids Using a One-Step, Near-Infrared-Assisted Evaporation Process

André Utgenannt,[a] Ross Maspero,[a,b] Andrea Fortini,[a] Rebecca Turner,[a] Marian Florescu,[a,b]

Christopher Jeynes,[c] Antonios G. Kanaras,[d] Otto L. Muskens,[d] Richard P. Sear,[a]

and Joseph L. Keddie[a*]

a. Department of Physics, University of Surrey, Guildford, Surrey GU2 7XH, UK

b. Advanced Technology Institute, University of Surrey, Guildford, Surrey GU2 7XH, UK

c. Ion Beam Centre, University of Surrey, Guildford, Surrey GU2 7XH, UK

d. Physics and Astronomy, Faculty of Physical Sciences and Engineering, University of Southampton, Highfield, Southampton, SO17 1BJ, UK

Quantitative Structural Analysis

ImageJ software was used to analyze SEM images to determine the center-to-center distance, L, of the polymer particles on the film surface and to determine the inner diameter of the holes in the grid, d_i. These spacing parameters as a function of $\sqrt{Pe_S Pe_L}$ are shown in Figures S1a and b for polymer particles of three different sizes (listed in Table S1). The meanings of L and d_i are defined in Figure S1c. In all hybrid structures, the values of L and d_i do not change significantly in the investigated range of evaporation rates and corresponding Pe.

For comparison to L, Table S1 shows the center-to-center distance in the reference samples, L_{Ref}, which are centre-to-centre distances measured in rapidly-dried polymer films that do not contain AuNPs. In Table S1, it can be seen that L_{Ref} is always larger than the true particle diameter, $d = 2R_L$, of the polymer particles. This is because these parameters were determined at different conditions. In order to obtain d by SEM, highly diluted dispersions of the appropriate latex were dried at room temperature, where the polymer particles will not deform because the T_g of the particles is higher. To obtain L_{Ref}, rapidly dried films without AuNPs were investigated. Because of the IR-heating to temperatures above T_g, the polymer particles are slightly flattened.

For all three particle sizes, L is slightly greater than L_{Ref} (less than 10 nm greater), which indicates that no more than a single AuNP layer is trapped between the polymer particles when they crystallize at the water/air interface. The polymer particles are slightly more flattened at the contact points in the Au nanogrid structure than in the reference samples. This can explain why L is not greater than L_{Ref} by exactly the distance of a AuNP diameter.

Table S1. Comparison of the true polymer particle diameter, d, with the center-to-center distance of the polymer particles in reference films, L_{Ref}, and in films containing AuNPs, L.

d	L_{Ref}	L	Size Ratio R_L/R_S
147 ± 6	150 ± 3	157 ± 3	14.1
261 ± 5	263 ± 4	269 ± 6	25.1
338 ± 5	346 ± 6	351 ± 2	32.5

Interestingly, the inner diameters of the holes, d_i, in the gold nanogrid are influenced very little by changes in the evaporation rate and remain almost constant within a series, as can be seen in Figure S1. Only the hybrid structure dried at the highest evaporation rate of the series with the highest R_L:R_S ratio shows a drop by 17 nm for d_i, whereas all other samples of the same series have a constant d_i. The lack of changes in the spacing parameters in the close-packed particle layers supports the idea that the polymer particles crystallize first at the water/air interface at an early stage in the drying process due to the higher capillary attraction between larger particles.
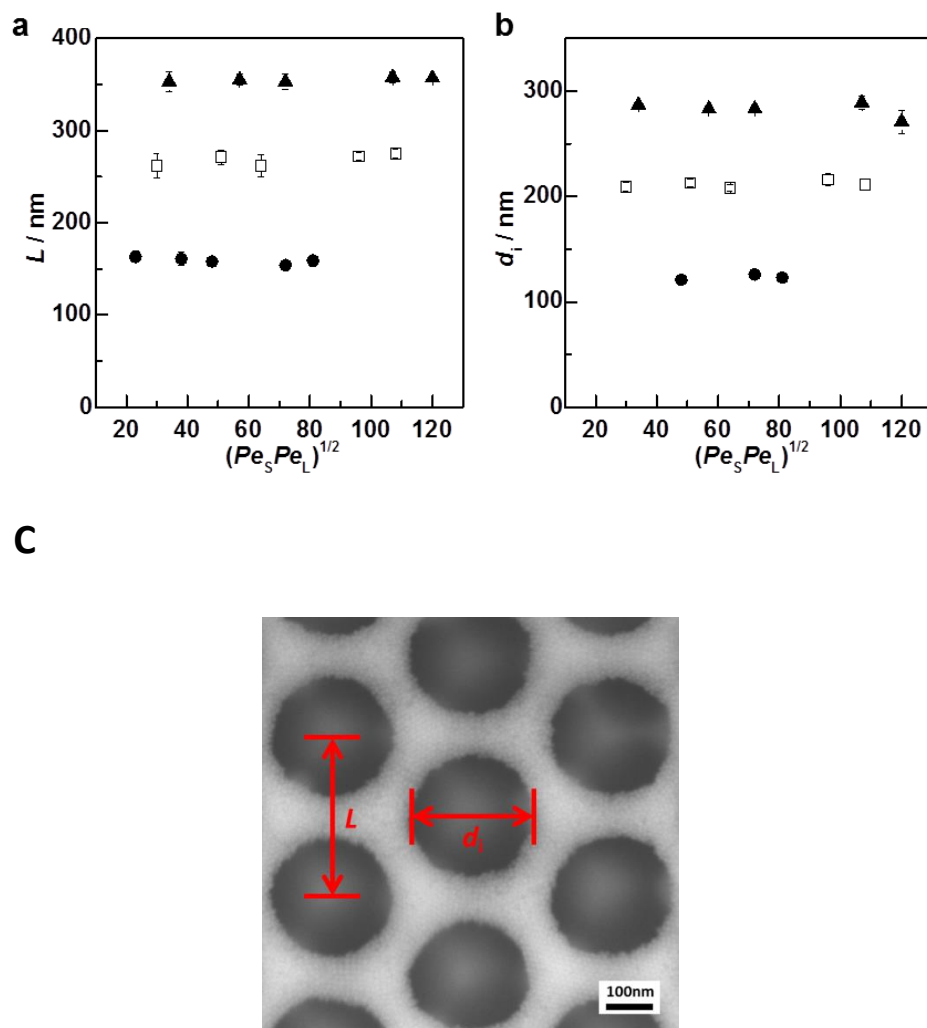
Figure S1. Spacing parameter in the nanogrid structure formed in rapidly dried films with the 10 nm AuNPs and three different polymer sizes, leading to R_L:R_S ratios of (▲) 32.5:1; (□) 25.1:1; and (●) 14.1:1. **a)** The centre-to-centre distance of the polymer particles, L, and **b)** the diameter of the holes in the grid, d_i, do not change significantly with evaporation rate and Peclet number. **c)** The definitions of the dimensions.

$\dot{E}$ (10^{-6} m s^{-1})
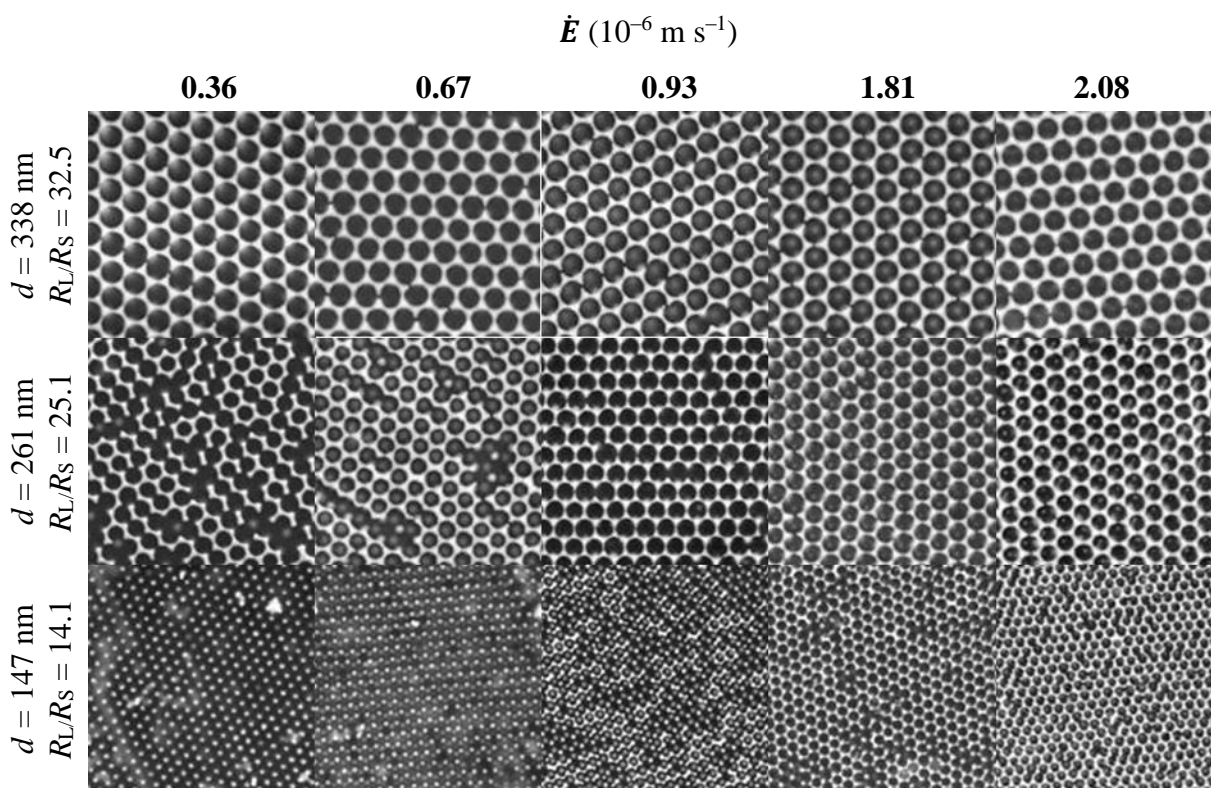
Figure S2. SEM analysis of nanostructures in rapidly dried hybrids. Particle blends with three different particle size ratios were dried under IR-radiation over a range of power densities to ah different evaporation rates, resulting in the evaporation rates shown along the top of the figures. The particle size ratios are given along the left side. All images represent a scanned area of 3 μm × 3 μm.

Quality Factor, Q, for the Nanostructures

In order to quantify the defects in a nanogrid structure, the quality factor, Q, is introduced. Here, a defect is defined as a misfit in the grid structure, for example, a missing bridge between rings. To calculate Q, the SEM images of a sample (taken from positions without grain boundaries) were analyzed using the particle analysis function of the image processing software ImageJ (1.47v,

available from the website http://imagej.nih.gov/ij of the National Institute of Health, USA) by the following method:

In the first step, the number of holes, h, in a grid without defects for a certain area, A, was calculated. The number of holes is given by the number of polymer particles, P, on the surface because each hole belongs to a polymer particle. Therefore, Thue's theorem[1] for the maximum coverage of a hexagonal circle packing, $\eta_h = \pi/(2\sqrt{3}) = 0.9069$ was used to calculate the maximum area that can be covered by the polymer particles (using the cross section of the polymer particles with the assumption that they are still spherical and not deformed). The number of holes was obtained when A_{max} is divided by the cross-sectional area of the polymer particles (πR^2) :

$h = P = A\eta_h / (\pi R^2)$

In the second step, the software was used to lay a mask over an image in order to count the number of holes without misfits, f. The parameters in the particle analysis function of the software were set in a way that only spherical holes that are not connected to a neighboring hole were considered. This can easily be done by setting the circularity to 0.7−1.0 and the area of the hole in a range close to the actual value. With this restriction, the area of connected holes is too large and therefore they are not counted. An original SEM image and the corresponding processed image for an area with a small number of defects are shown in Figure S2a and b. Original SEM and processed images for an area with many misfits are shown for comparison in Figure S2c and d.

The quality factor is defined as:

$$Q = \frac{f}{h}$$

For a grid structure with a very small number of defects (high quality), a value close to unity will be obtained for Q. On the other hand, a grid with poor quality will yield a value for Q close to zero.

This process was repeated at three randomly chosen positions to analyze a total of at least 3000 holes in the grid.
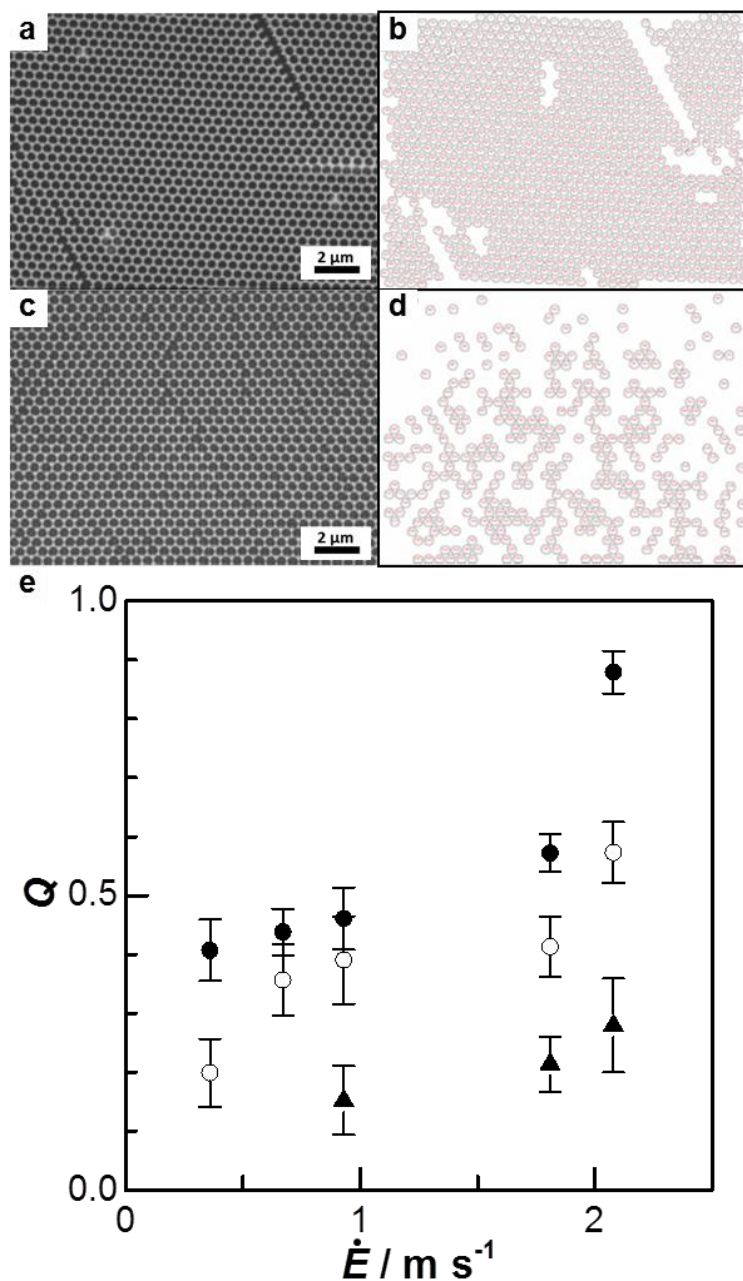
Figure S3. Determination of the grid quality, Q, as a function of the evaporation rate. **a)** An example of a SEM image which was processed by ImageJ by the method described in the text, resulting in **b)** an image where the positions of the grid without defects are counted. For comparison, **c)** the SEM image and **d)** the processed image of a sample surface with a low Q are shown, resulting in a small number of counted holes without misfits. **e)** A plot of Q as a

function of $\dot{E}$ for the particle blend films. The structures are made using 10 nm AuNPs and the three different polymer sizes, leading to R_L:R_S ratios of (▲) 14.1:1; (○) 25.1:1; and (●) 32.5:1.
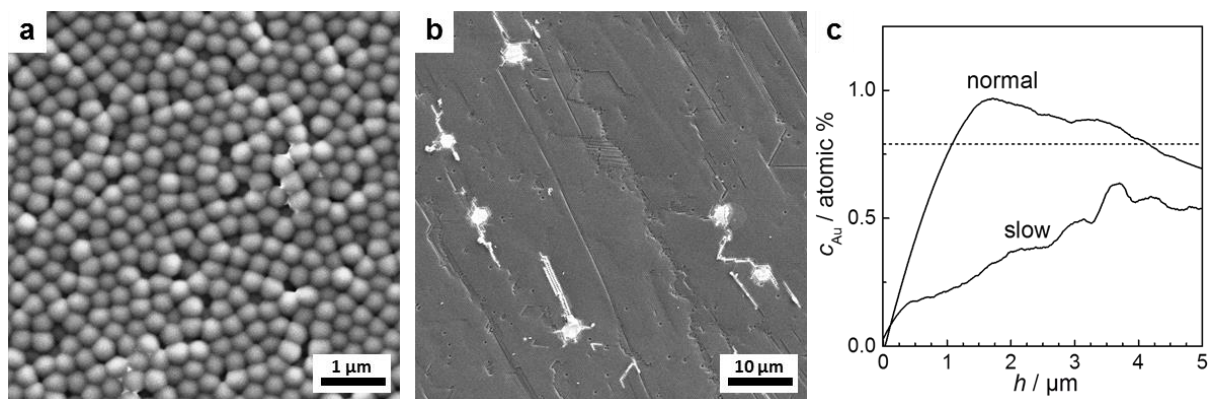
Figure S4. a) Representative SEM image of the surface structure after *normal* drying ($\dot{E}$ = 1.1 × 10^{-7} ms^{-1} and Pe$_S$ = 1.1). A limited number of AuNPs is observed as small white spots, and polymer particles are seen to be randomly packed. Scale bar is 1 μm. **b)** Representative SEM image of the surface structure after *slow* drying ($\dot{E}$ = 3.2 × 10^{-9} ms^{-1} and Pe$_S$ = 0.03). Aggregates of AuNPs in elongated crystals are seen in a few isolated areas. Scale bar is 10 μm. **c)** Au concentration depth profiles obtained from RBS analysis of structures dried at normal and slow rates (as indicated). The dashed line represents the concentration corresponding to a hypothetical homogenous distribution of the AuNPs.

Langevin Dynamics Simulations

We model a bimodal blend of N_s small spherical particles (AuNPs) of radius R_S and N_L large particles (polymer) with radius R_L suspended in water at a constant temperature T in a box with dimensions of $L_x \times L_y \times H$, where H represents the height of the initial layer. We use periodic boundary conditions in the x- and y-direction, while in the z-direction, the box is delimited at the bottom by a hard substrate, and at the top by a soft wall, which models the water/air interface.

The simulations were carried out using the LAMMPS simulation code[2] customized in order to include the model water/air interface. We do not explicitly simulate the solvent water molecules but describe the motion of the colloidal particles using Langevin dynamics, which includes Brownian diffusion effects and drag forces but neglects hydrodynamic flow. We have used 2×10^5 particles with a number ratio of $N_S{:}N_L$=212:1 and a size ratio $R_L{:}R_S$=32:1. These values were selected to agree closely with the experimental parameters. The height of the simulation box was H=24,000R_s while the lateral sizes were L_x=274 R_s and L_y=316 R_s. The time step was dt = 3×10^{-5} τ_B = 0.003 t_0, where τ_B is the Brownian time, and t_0 is the standard Lennard-Jones unit of time in LAMMPS. For the Langevin dynamics, we used a friction parameter $\xi = 1000$ and a temperature of 10, both in standard Lennard-Jones LAMMPS units.

The solvent evaporation process was modelled by a moving soft wall, which pushes the particles toward the bottom substrate at a constant rate $\dot{E} = 12\ R_s/\tau_B$, with $\tau_B = 4\ R_s^2/D_S$, where D_S is the Stokes-Einstein diffusion coefficient. Thus, for the small particles, Pe$_S$ = 7.2×10^4, and for the large particles, Pe$_L$ = 2.3×10^6. In the experiments, the Péclet numbers of both types of particle (AuNP and polymer) are much greater than one. Hence, the experiments and the simulations are both in the high-Pe limit. The Péclet numbers are larger in the simulation than in the experiment because

the run time of the simulation scales as one over Pe, and therefore simulating with a smaller Pe is not possible. The simulation was run for 41,000 t_0, and took 23,000 CPU hours.

The interaction between the soft wall and the particles is described by a harmonic potential given by $U_{aw}/k_BT = \frac{\alpha}{k_BT}(z - \xi - z_{int}(t))^2$, where $\frac{\alpha}{k_BT} = 1$ and 10^3 are the interaction strengths for the small and large particles, respectively. The vertical position of the interface time t is $z_{int}(t) = H - \dot{E}t$, while the parameter ξ is the distance of the particle center of mass to the water/air interface. (For particles trapped at the water/air interface, ξ is related to the contact angle θ of the water with respect to the solid particles by the relation $90° - \theta = \cos^{-1}\frac{\xi}{R_i}$, where R_i is the radius of the particle. See the diagram in Figure S6. A value of $\theta = 75°$ was used in the simulations.) The inter-particle potential energy U_{ij} between particles i and j is purely repulsive and defined as

$$U_{ij}/k_BT = \begin{cases} \frac{A}{k_BT}e^{-k(|r|-(R_i+R_{ij}))} & |r| < R_i + R_j \\ 0 & \text{otherwise} \end{cases},$$

where $A/k_BT = 2.5$ is the contact energy of the particles and $k = 40/R_s$ determines the steepness of the potential and $|r|$ is the center-to-center distance between the particles. The interaction between the particles and the bottom substrate is modelled by the repulsive potential

$$U_{i-\text{sub}}/k_BT = \begin{cases} 4.0\frac{\varepsilon}{k_BT}\left(\frac{2R_i}{z}\right)^{12} & z < R_i \\ 0 & \text{otherwise} \end{cases},$$

where $\frac{\varepsilon}{k_BT} = 10$ is the strength of the interaction and z is the distance of particle i from the substrate.
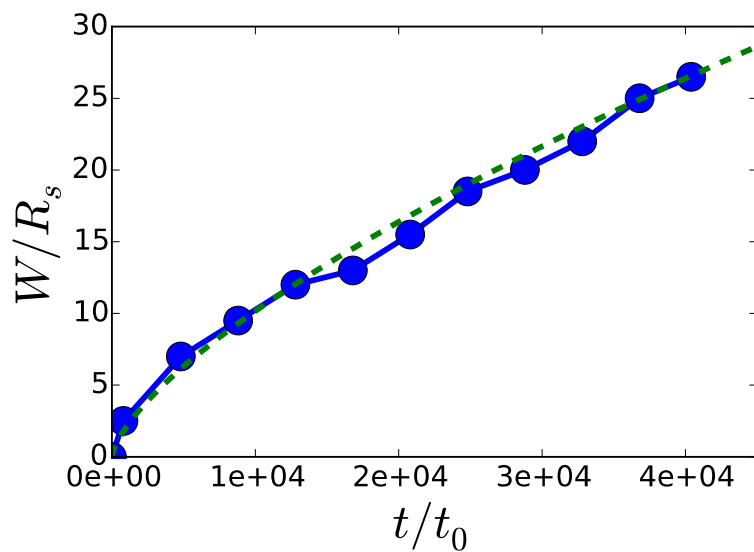
Figure S5. Width of the layer of small particles as a function of simulation time, measured in the simulation. Connected circles are the simulation results; the dashed line is the fitted function $W(t)/R_s=0.018 \ (t/t_0)^{0.688}$. The thickness W of the layer of small particles increases sub-linearly with time.
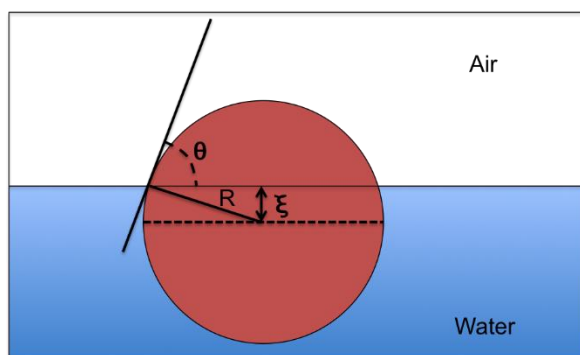
Figure S6. A diagram showing the relationship between the distance, ξ, and the contact angle, θ, for a particle at the water/air interface.

Movie 1. Langevin dynamics simulation of nanogrid formation. There are a total of 2×10^5 particles with a number ratio of $N_S{:}N_L{=}212{:}1$ and a size ratio of $R_L{:}R_S{=}32{:}1$. Each frame corresponds to a time increment of approximately $4.1\,\tau_B$. One second equals $12.4\,\tau_B$.
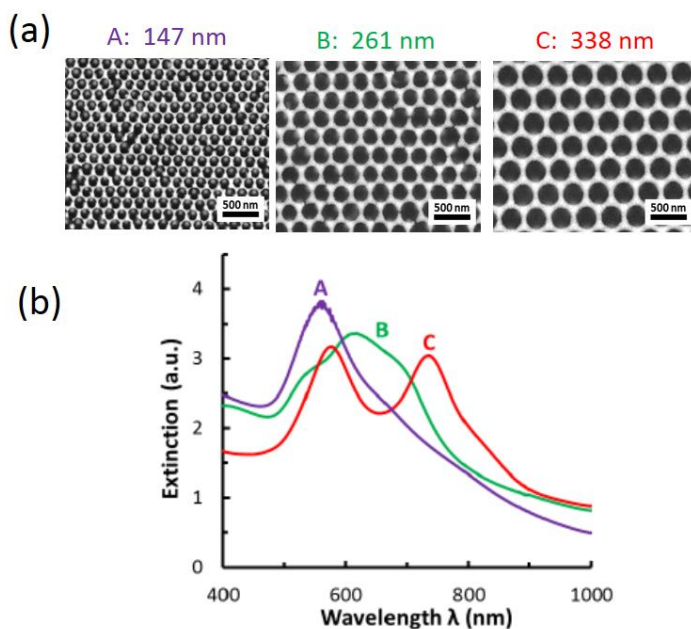
Figure S7. (a) SEM images of the nanogrid structures at the surface of hybrid films with increasing polymer particle sizes (left to right): (A) 147 nm, (B) 261 nm and (C) 338 nm. Samples were prepared with the fast evaporation rate under NIR radiation. (b) UV-Vis-NIR extinction spectra for these same three hybrid structures with increasing polymer particle sizes.

Plasmonic Resonances of the AuNP Nanogrid

We have modelled the AuNP nanogrid as a homogeneous medium with an effective dielectric constant defined by a renormalized Maxwell Garnett (MG) approach.[3] Explicitly, the effective permittivity of the Au nanogrid is defined[3] as:

$$\varepsilon_{\text{eff}} = \frac{\left[1+2f+(f-1)R^3G\right]\dfrac{\varepsilon_S}{\varepsilon_H}+2-2f+(1-f)R^3G}{\left[1-f+(f-1)R^3G\right]\dfrac{\varepsilon_S}{\varepsilon_H}+2+2f+(1-f)R^3G} \ .$$

Here, R is the NP radius, f is the filling ratio, ε_S is the NP permittivity, and ε_H is the dielectric background permittivity. The coupling coefficient G, accounting for the nearest neighbouring NP and radiative corrections up to the second order,[3] is given by:

$$G = \frac{k^2}{R} + \frac{2}{d^3}\left[1+k^2\frac{\left(15d^2-R^2\right)}{10}+\frac{3}{5}\frac{R^2}{d^2}\right].$$

where d is the average interparticle separation, and $k=2\pi/\lambda$ is the wavenumber.

The Au permittivity is modelled through the Drude-critical point model[4,5] by fitting the experimental data of Johnson and Christy.[6] We also account for the scattering of the Au conduction electrons from the AuNP surface and use a modified damping[7] given by: $\gamma(R)=\gamma_0\left(1+\dfrac{l_\infty}{l^*(R)}\right)$, where γ_0 and l_∞ are the damping and the mean free path of the electrons in bulk Au, respectively. $l^*(R)=\dfrac{R}{A}$ is the contribution brought about by the collisions of the conduction electrons with the NP surface, with A being a constant dependent on the details of the scattering processes considered.[7] In our simulations, we use $l_\infty=35.7\,\text{nm}$ (from ref. 7) and $A=0.33$ (from ref. 9). Figure S8 illustrates the refractive index values predicted by this renormalized MG approach.
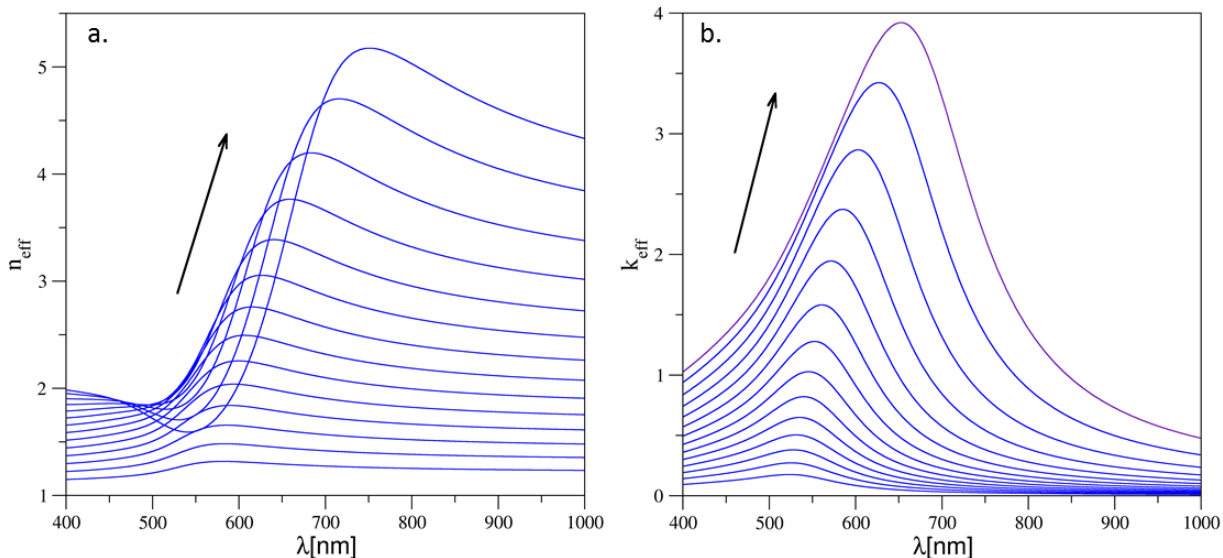
Figure S8. (a) Real and (b) imaginary components of the effective index of refraction of the AuNP homogenous material used in the simulations as a function of the filling ratio, increasing along the direction of the arrows from 0.1 to 0.74.

The system was then modelled as a closed-packed FCC lattice of polymer spheres with a refractive index of 1.47 and particle diameter of 338 nm. Homogeneous Au with an effective permittivity described above is then infiltrated in the voids to form an inverted opal structure. To make closer contact with the experimental configuration, we employ a graded Au filling and vary the filling ratio from 0.64 (topmost layer) to 0.25 (bottom layer). To build the protruding nanogrid structure (see Fig. 3d), we let the Au layer extend 40 nm above the polymer opal and then etch down with a triangular layer of closed-packed spheres aligned on top of the upper layer of polymer spheres. The resulting structure is schematically shown in Figure S9. To balance accuracy and computation costs we employ a 12-layer polymer opal.

All data files are available on the University of Surrey on-line publications repository: http://epubs.surrey.ac.uk
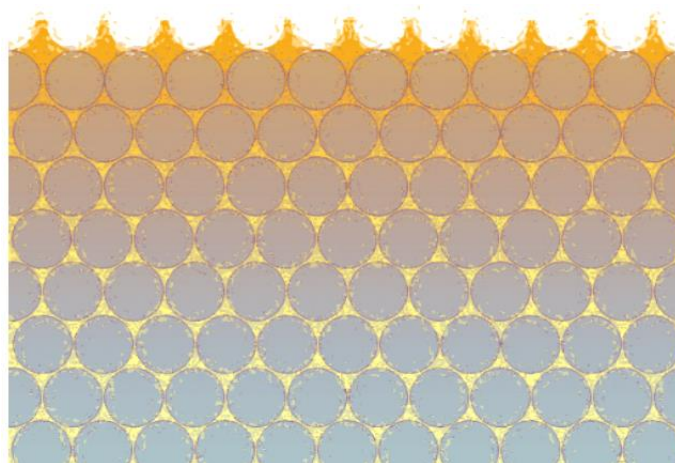
Figure S9. Schematic representation of the simulated structure. The structure consists of 12 polymer close-packed FCC layers infiltrated with homogeneous Au displaying a graded filing ratio along the vertical direction. The protruding nanogrid structure is built by etching a triangular layer of closed-packed spheres aligned with the topmost opal layer onto a homogeneous 40 nm Au layer sitting on top of the polymer opal.
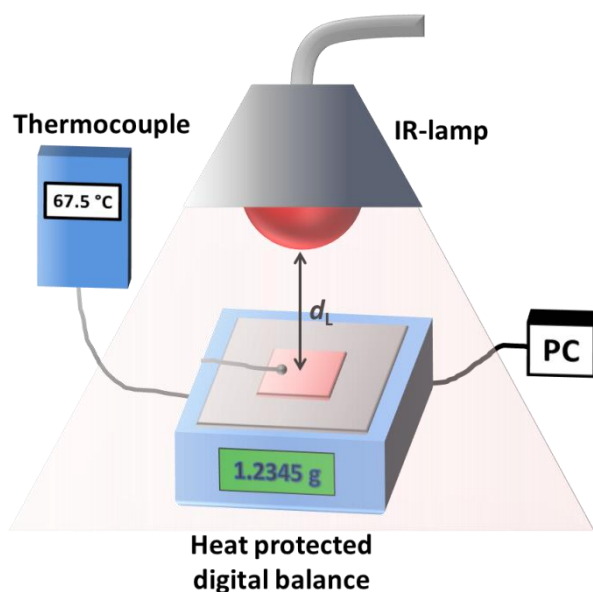
Figure S10. Experimental set-up for infrared-assisted film formation

Rutherford Backscattering Spectrometry Analysis

Figure 1e is drawn from the data in the file AU050101.dat that can be found in the folder "Utgenannt_RBS Data_IBA-8Oct2013", which is available on the University of Surrey on-line publications repository: http://epubs.surrey.ac.uk . These data were collected on 31st August 2013. The laboratory report for the analysis can be found in the file UtgenanntReport8Oct2013.pdf in the repository.

The figure shows the raw Au signal plotted as the absolute concentration as a function of depth from the surface, assuming the energy loss function given by the fit to the data. This fit is shown in the Report (p.8: "Auf0501"; data and fit), and the fitted depth profile of Au is shown in the figure below it. This profile was obtained with the number of layers limited so that the number of free parameters of the (model-free) fit are also limited. However, in this case we judge that this fixed number of layers is not sufficient to adequately represent the fine features in the data. Therefore, in Figure 1e we present the Au signal on the depth scale rather than the fit to the data.

References

1. Kreibig, U.; Genzel, U. Optical Absorption of Small Metallic Particles. *Surf. Sci.* **1985**, *156*, 678–700.

2. Plimpton, S. Fast Parallel Algorithms for Short-Range Molecular Dynamics, *J. Comp. Phys.* **1995**, *117*, 1-19.

3. Yoo, S; Park, Q-H. Effective Permittivity for Resonant Plasmonic Nanoparticle Systems *Via* Dressed Polarizability. *Opt. Express* **2012**, *20*, 16480–16489.

4. Vial, A. Implementation of the Critical Points Model in the Recursive Convolution Method for Modelling Dispersive Media with the Finite-Difference Time Domain Method. *J. Opt. A, Pure Appl. Opt.*, **2007**, *9*, 745–748.

5. Etchegoin, P. G.; Le Ru, E. C.; Meyer, A. An Analytic Model for the Optical Properties of Gold. *J. Chem. Phys*. **2006**, *125*, 164705.

6. Johnson, P. B.; Christy, R. W. Optical Constants of the Noble Metals, *Phys. Rev. B* **1972**, *6*, 4370–4379.

7. Hovek, H; Fritz, S: A. Hilger, A; Kreibig, U. Width of Cluster Plasmon Resonance: Bulk Dielectric Functions and Chemical Interface Damping, *Phys. Rev. B* **1993**, *48*, 181178–18188.

8. Noginov, M.; Podolskiy, V. *Tutorials in Metamaterials*; Taylor & Francis: Boca Raton, FL, **2012**.

9. Novo, C; Gomez, D; Perez-Juste, J; Zhang, Z; Petrova, H; Reismann, M; Mulvaney, P; Hartland, G. V. Contributions from Radiation Damping and Surface Scattering to the Linewidth of the Longitudinal Plasmon Band of Gold Nanorods: A Single Particle Study. *Phys. Chem. Chem. Phys*. **2006**, *8*, 3540-3546.